CrossMark

ORIGINAL PAPER

Magnetic and Electrical Properties of Magnesium-Substituted Ni–Zn Ferrites

N. Kavitha[1] · P. Manohar[1]

Abstract The effect of magnesium substitution in Ni–Zn ferrites ($Ni_{0.80-x}Mg_xZn_{0.20}Fe_2O_4$, where $x = 0$, 0.10–0.50) was studied on its electrical and magnetic properties. Ni–Mg–Zn ferrites were synthesized by novel combustion method, followed by calcination at 900 °C. The X-ray diffraction (XRD) pattern shows that the prepared sample was a single-phase spinel cubic structure, and the calculated crystallite sizes were found to be in the range 44–48 nm. Fourier transform infrared spectroscopy (FTIR) spectra confirm the tetrahedral and octahedral modes of vibrations. The observed saturation magnetization values range from 37 to 63 emu/g for magnesium-added Ni–Zn ferrites. The increase in resistivity was observed with the addition of magnesium ions except for the concentration of $x = 0.50$. The change in dielectric behavior with respect to composition and frequency were studied.

Keywords Ni–Mg–Zn ferrites · Combustion method · Magnetic properties · Dielectric properties

1 Introduction

Ferrites are one of the important materials which are used in technological applications mainly in electronics and telecommunication industries [1]. The significant electrical and magnetic properties of ferrites lead the material to be utilized in applications such as high-frequency transformer cores, antenna rods, loading coils in microwave devices, gas sensors, catalysts, and magnetic-drug delivery [2].

Ferrites having the general composition AB_2O_4 possess a spinel cubic close-packed structure which has two different interstitial positions (tetrahedral (A) and octahedral (B) sites). Among the various ferrites, spinel-structured soft Ni–Zn ferrites are mainly used and studied for their versatile nature in varying the properties with composition, method of synthesis, sintering condition, quantity, and type of additives and their distribution over tetrahedral (A) and octahedral (B) sites in the spinel structure [3].

Many researchers [3–5] studied the Ni–Zn ferrite properties by varying the composition. From the literature, it was observed that Ni–Zn ferrites with the composition of $Ni_{0.80}Zn_{0.20}Fe_2O_4$ possess superior property. Incorporating new elements into the $Ni_{0.80}Zn_{0.20}Fe_2O_4$ system, the magnetic and dielectric properties can be tailored. Among the various elements incorporated in the Ni–Zn ferrite system, not a significant amount of work is focused on Mg^{2+} ion substitution. It has been found from the work of different researchers that the Mg^{2+} ion-substituted ferrite system shows enhancement in properties such as improved saturation magnetization and resistivity, reduction in power loss, and also good thermal stability [6–9]. Hence, the work in this paper is focused on tailoring this composition by substituting various concentrations of Mg^{2+} ions in the place of Ni^{2+} ion to study the effect of magnesium on electrical and magnetic properties.
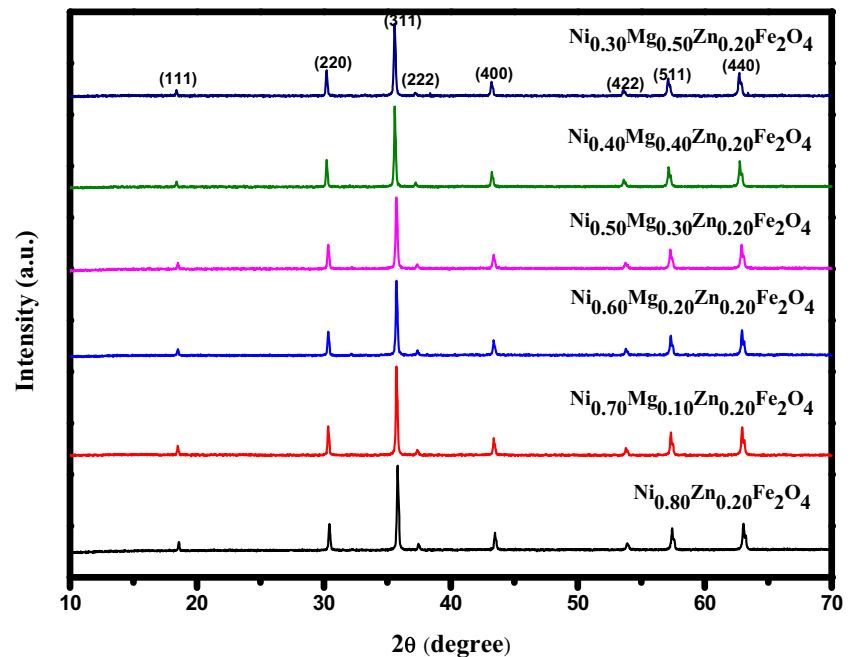
2 Experimental

Ni–Mg–Zn ferrite powders with the composition $Ni_{0.80-x}Mg_xZn_{0.20}Fe_2O_4$ were prepared using the flash combustion method [10]. Nickel nitrate, magnesium nitrate,

✉ P. Manohar
pmano@annauniv.edu

[1] Department of Ceramic Technology, Anna University, A.C.Tech campus, Chennai, 600025, India

Fig. 1 XRD patterns of calcined $Ni_{0.80-x}Mg_xZn_{0.20}Fe_2O_4$ powders

zinc nitrate, and iron III nitrate were used as the precursor materials. Citric acid was chosen as the fuel material. All the chemicals were measured with respect to their stoichiometric proportion. The metal-to-citric acid ratio was maintained at one to obtain a complete combustion process. A minimum amount of water is added to the nitrate–citric acid mixture and made to stir on the magnetic stirrer at the temperature of 80 °C until the metal nitrate/citric acid solution is transformed into a gel. The gel is transferred to an alumina crucible and is kept in a preheated furnace at 500 °C. The combustion process takes place within few seconds with the release of a large amount of heat and fumes which results in fluffy burnt ash. The burnt ash is collected and crushed using a mortar and pestle.

The resultant ground powder was calcined at 900 °C for 2 h. The structure and phase of calcined powders were identified using a powder X-ray diffractometer (Bruker D2 phaser) with CuK α radiation in the Bragg angle range of 10° to 70°. FTIR spectra were recorded from a Fourier transform infrared spectrometer (Perkin Elmer Spectrum RX I model) to study the phase formation using a KBr pellet. Room temperature magnetic measurements were obtained using a vibrating sample magnetometer (Lakeshore VSM 7410) at the field range of +15000 to −15000 Oe. Impedance measurements were carried out in the frequency range of 1 kHz to 3 MHz at room temperature using a phase-sensitive multi-meter with impedance analysis interface (Numetriq PSM-1735, UK).

3 Results and Discussion

3.1 XRD Analysis

X-ray diffraction (XRD) analysis of ferrites helps to identify the structure and purity of the materials prepared. Figure 1 shows the XRD pattern of calcined samples with different composition. The characteristic planes (220), (311), (222), (400), (422), (511), and (440) are seen in all the prepared samples, which show that all the samples have a single-phase spinel cubic structure [10, 11]. No other peaks corresponding to other phases are observed for all the samples. Crystallite size was calculated using the Debye–Scherrer formula,

$$D = 0.9\lambda/\beta\cos\theta$$

where D is the crystallite size, λ the wavelength of the X-ray, β the full width at half maximum of the reflection line, and θ the Bragg angle. The lattice constants (a) of all the samples were calculated using the relation

$$a = d_{hkl}/(h^2 + k^2 + l^2)^{1/2}$$

and are tabulated in Table 1, which very well agreed with the previous results done by different researchers. The X-ray density ($\rho_{X\text{-ray}}$) was calculated from the relation

$$\rho_{X\text{-ray}} = 8M/Na^3$$

Table 1 Structural parameters from XRD data

Mg concentration	Crystallite size (nm)	Lattice constant (Å)	d spacing (Å)	X-ray density (g/cm^3)
$x = 0.00$	47.73	8.3075	2.5048	5.4540
$x = 0.10$	48.81	8.3274	2.5108	5.2963
$x = 0.20$	47.27	8.3281	2.5110	5.2159
$x = 0.30$	44.90	8.3295	2.5114	5.0808
$x = 0.40$	45.88	8.3586	2.5202	5.0025
$x = 0.50$	45.97	8.3618	2.5211	4.9187

where M is the molecular weight, N the Avogadro number, and a the lattice constant. The average crystallite size values range between 44 and 48 nm. The values of the lattice constant and X-ray density were calculated using XRD data and are tabulated in Table 1. The lattice constant values increase as there is an increase in magnesium concentration, due to the replacement of a lesser ionic radius of Ni^{2+} by a larger ionic radius of Mg^{2+}. The X-ray density of the prepared samples decreases with an increase in the magnesium concentration because lesser-density magnesium ion is substituted for high-density nickel ions [12].

3.2 FTIR Analysis

In general, the existence of two wide bands between 600 and 400 cm^{-1} indicates the formation of single-phase spinel ferrites [13]. The FTIR spectra were observed in the frequency range from 400 to 1000 cm^{-1} and are shown in Fig. 2. The two major characteristic peaks are observed between 600 and 400 cm^{-1} which confirms the formation of the spinel structure in all the prepared samples. The peak
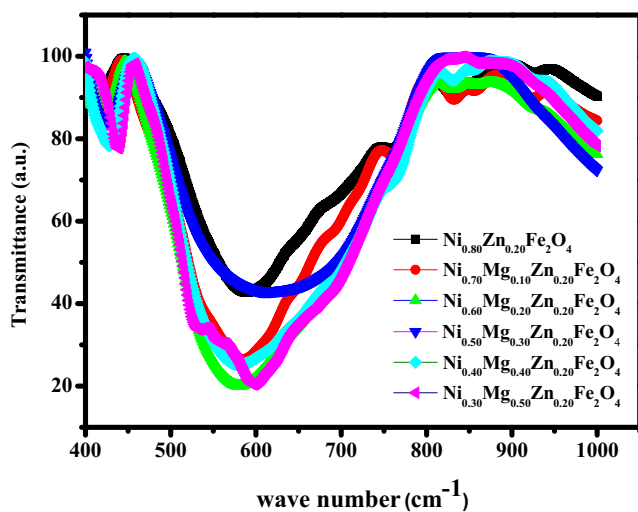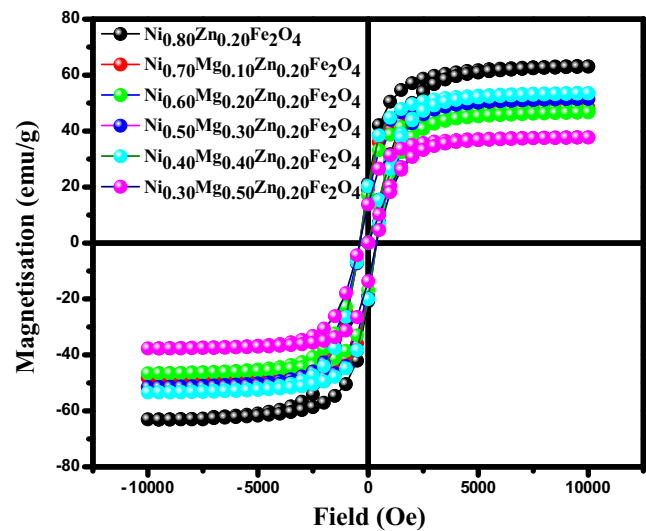

Fig. 3 Room temperature hysteresis loop of calcined $Ni_{0.80-x}Mg_xZn_{0.20}Fe_2O_4$ powders

around 600 cm^{-1} ($v1$) corresponds to the tetrahedral mode of vibration (Mtetra—O). The band frequency is high for tetrahedral vibration because the bond length (Mtetra—O) is small which gives more covalent nature and leads to high-frequency vibrations. The peak around 400 cm^{-1} ($v2$) is attributed to the octahedral mode of vibrations (Mocta—O). In this case, the bond length is larger compared to the tetrahedral mode of vibrations which corresponds to the lower-frequency vibrations of metal oxygen complexes [14, 15].

3.3 Magnetic Properties

The magnetic nature of the prepared ferrite samples was analyzed using a vibrating sample magnetometer (VSM), and its room temperature M-H loops are presented in Fig. 3. The values of saturation magnetization (M_s) and coercivities

Fig. 2 FTIR spectra of calcined $Ni_{0.80-x}Mg_xZn_{0.20}Fe_2O_4$ powders

Table 2 Variation of crystallite size, saturation magnetization, and coercivity values with composition

Mg concentration	Crystallite size (nm)	M_s (emu/g)	H_c (Oe)
$x = 0$	47.73	63.81	378.15
$x = 0.10$	48.81	48.75	384.67
$x = 0.20$	47.27	47.54	362.64
$x = 0.30$	44.90	51.55	366.54
$x = 0.40$	45.88	53.57	389.54
$x = 0.50$	45.97	37.74	381.81

(H_c) are tabulated in Table 2. All the samples show a soft-ferrite nature at room temperature. In general, the addition of Mg^{2+} ions in the place of Ni^{2+} ions decreases the saturation magnetization value due to the zero magnetic moment of the Mg^{2+} ion. From Fig. 3 and Table 2, it can be seen that addition of the Mg^{2+} ion decreases the magnetization value initially for the composition $x = 0.10$ and 0.20; then, the saturation magnetization increases up to $x = 0.40$. As the concentration is increased further to $x = 0.50$, the saturation magnetization value decreases to 37.74 emu/g.

The variation of saturation magnetization values can be explained by the distribution of cations among the tetrahedral (A) and octahedral (B) sites according to Neel's two-sublattice model. With respect to this model, there are three types of interaction that takes place between A and B sites which are A–A, B–B, and A–B interactions. Among the three, the A–B interaction is the strongest one. Hence, the net magnetization of a unit cell can be calculated from the difference between the magnetic moments of A and B sites. In Ni-Zn ferrites, the Zn^{2+} ion has the strong preference to occupy A sites. Ni^{2+} ions and Mg^{2+} ions mainly occupy B sites. Fe^{3+} ions have equal preference to occupy available A and B sites [16].

With this in mind, the anomalous nature of saturation magnetization with varying Mg^{2+} ion substitution can be explained by Neel's two-sublattice model. For the concentration of $x = 0.10$ and 0.20, there is a decrease in the saturation magnetization value compared with $x = 0$. The decrease in saturation magnetization is due to the replacement of high-magnetic-moment ($2\,\mu B$) Ni^{2+} ions by zero-magnetic-moment Mg^{2+} ions at octahedral (B) sites. This reduces the net magnetization of B sites which results in the reduction of the net magnetization of the unit cell according to Neel's two-sublattice model. A further increase in Mg^{2+} ion concentration ($x = 0.30$ and 0.40) increases the saturation magnetization value. This can be attributed to the redistribution of cations among A and B sites in which some of the Mg^{2+} ($0\,\mu B$) ions displace Fe^{3+} ($5\,\mu B$) ions from the A site to the B site which enhances the net magnetization of B sites and results in an increased value of saturation magnetization [12]. The excess addition of Mg^{2+} ions ($x = 0.50$) dilutes the magnetic moments of A and B sites, and their interactions become weaker; this leads to a lower value of saturation magnetization of 37.74 emu/g [7].

There is not much difference in the coercivity (H_c) value for all concentrations of Mg^{2+} ion incorporation, which concludes that the addition of Mg^{2+} ions does not induce the anisotropy nature in the crystal lattice. The H_c values range around 360–385 Oe. The low values of coercivity indicate the soft nature (easy to magnetize and demagnetize) of ferrites, and it suggests that it can be used in high-density data storage devices [17].
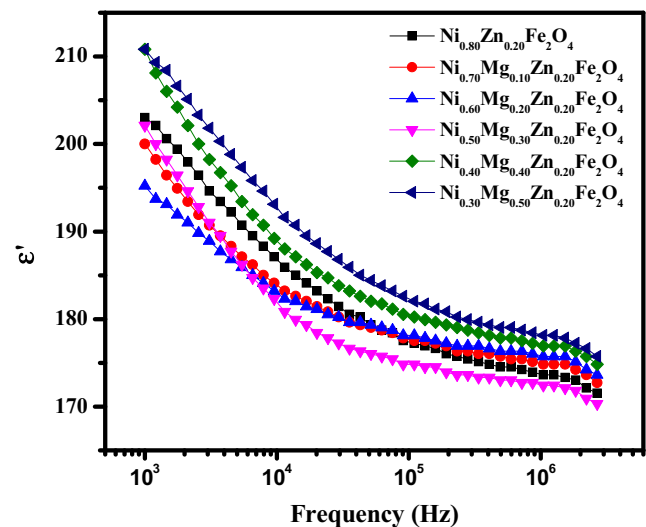

Fig. 4 Variation of the dielectric constant with frequency and composition

3.4 Dielectric Properties

3.4.1 Dielectric Constant

The variation of the dielectric constant with frequency is presented in Fig. 4. It shows the normal dispersion behavior of ferrites with increase in frequency. The dielectric constant decreases as the frequency of the applied field increases in the low-frequency region and at higher frequencies; it shows almost frequency-independent behavior [18]. The dispersion behavior can be explained by Koop's phenomenological theory based on the Maxwell–Wagner two-layer model for the inhomogeneous structure of ferrites. According to this model, polycrystalline ferrites consist of two layers possessing well-conducting grains and are separated by poorly conducting grain boundaries [19]. The polarization in ferrites occurs due to the availability of same ions with different valance states which leads to hopping of electrons between them. In general, presence of Fe^{3+} and Fe^{2+} ions in the ferrites at the B sites creates hopping of electrons between them and hence, displacement of electrons in the direction of the applied field. This results in polarization of ferrites [20]. At lower frequencies, the exchange of electrons between Fe^{3+} and Fe^{2+} ions follows the applied field frequency and contributes to the higher values of dielectric constant. The large dielectric constant values at low frequencies can also be related to the interfacial dislocation pileup, oxygen vacancies, grain-boundary defects, and so on. Beyond a certain frequency that is at higher frequencies, the exchange of electrons between Fe^{3+} and Fe^{2+} ions could not follow the applied alternating field [21].

Dielectric constant values at lower frequencies decrease as the concentration of Mg^{2+} ions increases up to $x = 0.30$. For the higher concentration (greater than 0.30) of Mg^{2+} ions, the dielectric constant value increases. The initial decrease in the dielectric constant can be attributed to the decrease in the electron exchange between Fe^{3+} and Fe^{2+} ions [22]. The presence of Fe^{2+} ions in excess amount which is formed during sintering can induce hopping of electrons between Fe^{3+} and Fe^{2+} ions which results in higher dielectric constant values for the samples with higher concentration (greater than $x = 0.30$.) of Mg^{2+} ions [10, 23].

3.4.2 Loss Factor Tan δ

The variation of tan δ with respect to frequency at room temperature is shown in Fig. 5. The dielectric loss factor tan $δ = ε''/ε'$ conveys the ability of the dielectric material that can convert electrical energy into thermal energy which produces heat in the material [24]. This arises because of the lag between polarization and applied field which is created by the impurities and imperfections in the crystal lattice [10]. The tan δ value continuously decreases as the frequency increases and reaches the constant value at higher frequencies. All the prepared samples show this normal dispersive behavior for ferrites. The species which is responsible for polarization such as Fe^{2+} content, impurities, and defects mainly decided by composition and its sintering temperature. It requires more energy to overcome high-resistive grain boundaries at low frequencies which results in higher values of the loss factor. At high frequencies, the energy required to transfer electrons between the ferric and ferrous
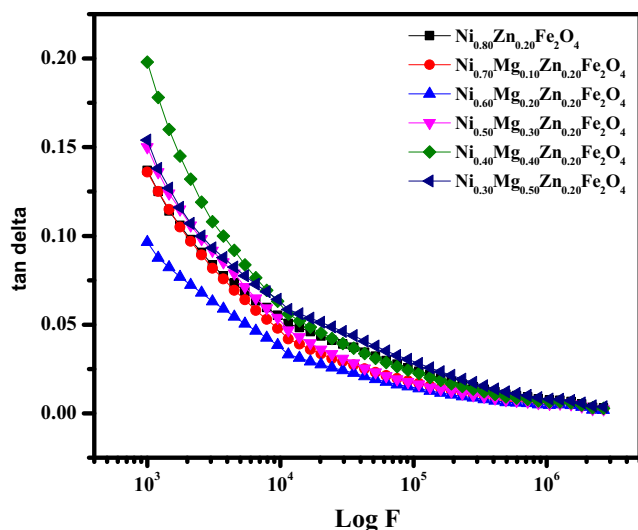
ions is less within the grain so that a decrease in the energy loss can be observed [25].

3.4.3 Impedance Analysis

Figure 6 shows the graph between the real and the imaginary part of impedance (Cole–Cole or Nyquist plot). In general, this plot is used to identify the various components such as grain, grain-boundary, and electrode contribution to the impedance of the material and its effects appear as semi circles. The lower- and higher-frequency semicircles can be related to grain-boundary and grain contribution [26]. The complex impedance plot shows that only one incomplete semicircular arc is obtained for all the concentration of Mg^{2+} ion substitution. This incomplete semicircle indicates the high resistivity of the material. It shows the overlapping of grain and grain-boundary effects [17, 27].

3.4.4 AC Conductivity

The variation of AC conductivity with frequency is shown in Fig. 7 for all the prepared samples. The increase in the AC conductivity is observed as the frequency of the applied field increases. The increase in frequency of the applied field increases more the number of electrons to be participated in the hopping mechanism which attributes to the increase of AC conductivity [28]. The conduction in ferrites at low frequency is due to the high-resistive grain-boundary effect which hinders the hopping of electrons, hence low conductivity. The high conductivity at high frequency is due to less-resistive grains [29]. From Fig. 7, it can be seen that the increase in Mg^{2+} concentration initially decreases
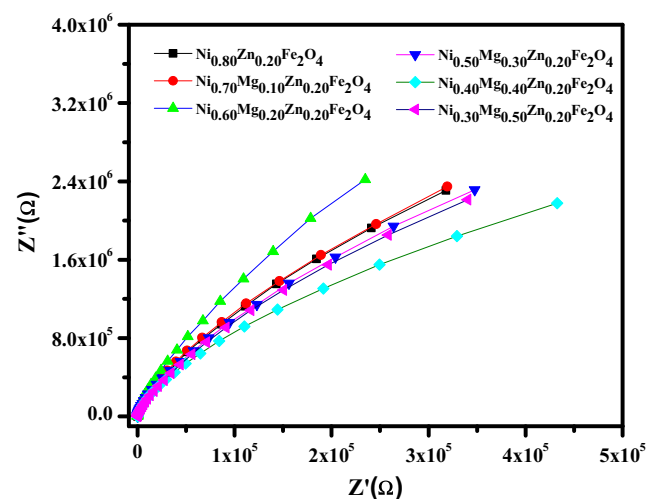

Fig. 5 Variation of tan δ (loss factor) with frequency and composition

Fig. 6 Complex impedance (Cole–Cole) plot of $Ni_{0.80-x}Mg_xZn_{0.20}Fe_2O_4$ pellets sintered at 1000 °C
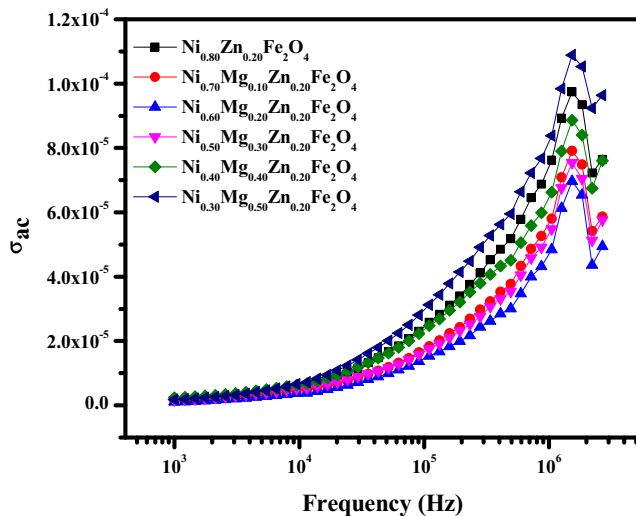
Fig. 7 Variation of AC conductivity with frequency and composition

the AC conductivity and, for higher concentration, conductivity increases. This can be explained by considering the distribution of cations among the available A and B sites. The replacement of Ni^{2+} ions by Mg^{2+} ions at B sites reduces hopping of electrons between Fe^{3+} and Fe^{2+} ions, and also, a decrease of Ni^{2+} ions at B sites also reduces hopping of holes between Ni^{3+}ions and Ni^{2+} ions and, hence, the conductivity decreases as the Mg^{2+} ion concentration increases initially. As the Mg^{2+} ion concentration increases, the Mg^{2+} ion occupies A sites and replaces some of the Fe^{3+} ions from the A sites to B sites which correspondingly increases the Fe^{3+} and Fe^{2+} ion concentration at B sites resulting in an increase in the hopping of electrons and hence an increase in conductivity [30]. It is therefore concluded that the sample with $x = 0.50$ has higher conductivity due to the availability of more Fe^{3+} and Fe^{2+} ions at B sites due to Mg^{2+} ion substitution and the sintering effect.

4 Conclusion

Ni–Mg–Zn ferrite powders with the composition $Ni_{0.80-x}Mg_xZn_{0.20}Fe_2O_4$ (where $x = 0.0$, 0.10, 0.20, 0.30, 0.40, 0.50) were synthesized with crystallite size ranges around 44–48 nm using the flash combustion method. XRD results confirmed that all the prepared samples were with the single-phase spinel cubic structure. FTIR results also confirm the spinel structure of all the samples with the characteristic peaks between 400 and 600 cm^{-1}. The substitution of magnesium ions for nickel ions reduces the magnetization for the initial concentration and the saturation magnetization value increases. The variation in saturation magnetization values was explained using the

redistribution of cations among available sites with Neel's two-sublattice model. Excess addition of magnesium ions dilutes the magnetic moment of A and B sites which reduces the net magnetization value. The dielectric study revealed the dependence nature of dielectric constant, loss factor, and AC conductivity with an increase in frequency. The addition of magnesium ions decreases AC conductivity values which shows the increase in resistivity except for the concentration $x = 0.50$. The samples with increased resistivity and higher magnetization values suggest that it can be used in high-frequency applications. The lower values of coercivity also suggest that the material can also be used in high-density data storage applications.

References

1. Varma, V., Pandey, V., Shukla, V.N., Annapoorni, S., Kotnala, R.K.: Solid State Commun. **149**, 1726–1730 (2009)
2. Druc, A.C., Borhan, A.I., Diaconu, A., Iordan, A.R., Nedelcu, G.G., Leontie, L., Palamaru, M.N.: Ceram. Int. **40**, 13573–13578 (2014)
3. Mangalaraja, R.V., Ananthakumar, S., Manohar, P., Gnanam, F.D.: Mater. Lett. **57**, 2662–2665 (2003)
4. Priyadharshini, P., Pradeep, A., Chandrasekaran, G.: J. Magn. Magn. Mater. **321**, 1898–1903 (2009)
5. Verma, A., Goel, T.C., Mendiratta, R.G., Gupta, R.G.: J. Magn. Magn. Mater. **192**, 271–276 (1999)
6. GangaSamy, D.R.S., Varma, C., Bharadwaj, S., Sambasiva Rao, K., Rao, K.H.: J. Supercond. Nov. Magn. doi:10.1007/s10948-015-3188-I
7. Abdullah Dar, M., Varma, V., Gairola, S.P., Siddique, W.A., Singh, R.K., Kotnala, R.K.: Appl. Surf. Sci. **258**, 5342–5347 (2012)
8. Singh, N., Agarwal, A., Sanghi, S., Khasa, S.: J. Magn. Magn. Mater. **324**, 2506–2511 (2012)
9. Sujatha, C., Venugopal Reddy, K., Gowri Babu, S., Reddy, R., Rao, K.H.: Physica B **407**, 1232–1237 (2012)
10. Mangalaraja, R.V., Ananthakumar, S., Manohar, P., Gnanam, F.D.: Mater. Lett. **57**, 1151–1155 (2003)
11. Singh, N., Agarwal, A., Sanghi, S., Singh, P.: Physica B **406**, 687–692 (2011)
12. Gabal, M.A.: J. Magn. Magn. Mater. **321**, 3144–3148 (2009)
13. Amer, M.A., Tawfik, A., Mostafa, A.G., El-Shora, A.F., Zaki, S.M.: J. Magn. Magn. Mater. **323**, 1445–1452 (2011)
14. Siva Ram Prasad, M., Rajesh Babu, B., Ramesh, K.V., Trinath, K.: J. Supercond. Nov. Magn. **27**, 2735–2745 (2014)
15. Manoj Kothawale, M., Tangsali, R.B., Naik, G.K., Budkuley, J.S.: J. Supercond. Nov. Magn. **25**, 1907–1911 (2012)
16. Ghodake, J.S., Kamble, R.C., Salvi, S.V., Sawant, S.R., Suryavanshi, S.S.: J. Alloys Compd. **486**, 830–834 (2009)
17. Kadam, A.A., Shinde, S.S., Yadav, S.P., Patil, P.S., Rajpure, K.Y.: J. Magn. Magn. Mater. **329**, 59–64 (2013)
18. Kotnala, R.K., Ahmad, S., Arham Ahmed, S., Shah, J., Azam, A.: J. Appl. Phys. **112**, 054323 (2012)
19. Anwar, H., Maqsood, A.: J. Supercond. Nov. Magn. **25**, 1913–1920 (2012)
20. Maqsood, A., Khan, K., Anis-ur-Rehman, M., Malik, M.A.: J. Supercond. Nov. Magn. **24**, 617–622 (2011)
21. Khan, K., Maqsood, A., Anis-ur-Rehman, M., Malik, M.A., Akram, M.: J. Supercond. Nov. Magn. **25**, 2707–2711 (2012)

22. Pervaiz, E., Gul, I.H.: J. Magn. Magn. Mater. **349**, 27–34 (2014)
23. Sujatha, C.h., Venugopal Reddy, K., Gowri Babu, S., Ramachandra Reddy, R., Buchi Suresh, M., Rao, K.H.: J. Magn. Magn. Mater. **340**, 38–45 (2013)
24. Loyau, V., Wang, G.Y., Lo Bue, M., Mazaleyrat, F.: J. Appl. Phys. **111**, 053928 (2012)
25. Iqbal, M.J., Ahmad, Z., Meydan, T., Melikhov, Y.: J. Appl. Phys. **111**, 033906 (2012)
26. Ramesh, B., Ramesh, S., Vijaya Kumar, R., Lakshmipathi Rao, M.: J. Alloys Compd. **513**, 289–293 (2012)
27. Batoo, K.M., Abd El-Sadek, M.S.: J. Alloys Compd. **566**, 112–119 (2013)
28. Hankare, P.P.: J. Magn. Magn. Mater. **323**, 389–393 (2011)
29. Anwar, Asghari Maqsood, H.: J. Magn. Magn. Mater. **333**, 46–52 (2013)
30. Batoo, K.M., Kumar, S., Lee, C.G., Alimuddin.: Curr. Appl. Phys. **9**, 826–832 (2009)